

Article

# Characterization of the Inlet Port Flow under Steady-State Conditions Using PIV and POD

Mohammed El-Adawy <sup>1</sup> , Morgan R. Heikal <sup>1,2</sup>, A. Rashid A. Aziz <sup>1,\*</sup>,  
Muhammad I. Siddiqui <sup>1,3</sup> and Shahzad Munir <sup>1,4</sup>

<sup>1</sup> Mechanical Engineering Department, Universiti Teknologi PETRONAS, 32610 Seri Iskandar, Perak, Malaysia; engmohammed\_2008@yahoo.com (M.E.-A.); M.R.Heikal@brighton.ac.uk (M.R.H.); muhammad.israr@utp.edu.my (M.I.S.); shahzad.munir@utp.edu.my (S.M.)

<sup>2</sup> Advanced Engineering Centre, School of Computing, Engineering and Mathematics, University of Brighton, Brighton BN2 4GJ, UK

<sup>3</sup> Nust Institute of Civil Engineering (NICE), National University of Science and Technology (NUST), 44000 Islamabad, Pakistan

<sup>4</sup> Department of Mathematics, COMSATS Institute of Information Technology, park road, chak shehzad campus, tarlai kalan, 44000 Islamabad, Pakistan

\* Correspondence: kotb\_g03443@utp.edu.my; Tel.: +60-183537595

Received: 18 October 2017; Accepted: 9 November 2017; Published: 24 November 2017

**Abstract:** The current study demonstrates an experimental investigation of the tumble flow structures using Particle Image Velocimetry (PIV) under steady-state conditions considering the central vertical tumble plane. The experiments were carried out on a four-valve, pent-roof Gasoline Direct Injection (GDI) engine head at different valve lifts and with a pressure difference of 150 mmH<sub>2</sub>O across the intake valves. Furthermore, the Proper Orthogonal Decomposition (POD) analytical technique was applied to PIV-measured velocity vector maps to characterize the flow structures at various valve lifts, and hence the different rig tumble values. The results show that at low valve lifts (1 to 5 mm), 48.9 to 46.6% of the flow energy is concentrated in the large (mode 1) eddies with only 8.4 to 11.46% in mode 2 and 7.2 to 7.5 in mode 3. At high valve lifts, it can be clearly seen that some of the energy in the large eddies of mode 1 is transferred to the smaller flow structures of modes 2 and 3. This can be clearly seen at valve lift 10 mm where the values of the flow energy were 40.6%, 17.3%, and 8.0% for modes 1, 2, and 3, respectively.

**Keywords:** GDI engine; tumble motion; PIV; flow bench; POD

## 1. Introduction

The automotive industry is increasingly motivated by high fuel economy demands and strict pollutant emissions regulations, hence there is a pressing need for novel combustion systems to meet these demands. One of the most promising internal combustion engine (ICE) designs for achieving a major part of these goals is the Gasoline Direct Injection (GDI) engine. GDI engines potentially offer several considerable advantages relative to port fuel injection (PFI) engines in terms of preventing the fuel wall film in the intake port and reducing the throttling losses (pumping losses) while providing higher thermal efficiency, higher compression ratios, lower fuel consumption, lower CO<sub>2</sub> and HC emissions, and higher volumetric efficiency [1,2]. GDI engines can be operated in either stratified charge mode or homogenous charge mode. A stratified charge mode (late injection) is utilized at lower engine speeds and loads as the fuel is injected late during the compression stroke. This mode enables engines to burn global very lean mixtures with very high air/fuel ratios, which cannot be achieved using multi point port fuel injection. However, more NO<sub>x</sub> emissions are generated due to the lean burn. Therefore, exhaust gas recirculation (EGR) is used during this mode to reduce the

NO<sub>x</sub> emissions. A homogenous charge mode (early injection) is preferred for higher loads and higher engine speeds. The fuel is injected early during the intake stroke so more time is available for air-fuel mixture formation. During this mode of operations, the engine operates with a near stoichiometric mixture which, in turn, decreases NO<sub>x</sub> emissions, and thus EGR is not used [3–6]. The main issue is to achieve these kinds of mixture modes with different in-cylinder flow structures under these operating conditions, which control the mixture formation. Many studies were carried out to solve these issues through the proper design of the combustion chamber, as well as the development of GDI spray systems and injector characteristics [7–15]. Another key approach was to make practical and effective use of the full potential of the characteristics of the in-cylinder flow field. Promoting the correct in-cylinder flow field is considered to be an effective method for controlling the mixture preparation in order to achieve rapid flame propagation, and hence improved engine performance [16]. In-cylinder flow structures can be divided into two basic fluid motions: swirl and tumble. The in-cylinder flow where the flow rotational axis is parallel to the cylinder is represented as a swirl and is usually targeted in compression ignition engines. On the other hand, the flow with an axis perpendicular to that of the cylinder axis is denoted as tumble and is typically targeted in pent-roof, four-valve spark ignition engines [17]. These coherent structures, either swirl or tumble, are reliant on the particulars of the bore/stroke ratio, the intake valve geometry, the inlet port profile, and the shape of the combustion chamber [18,19]. It is well known that one of the major issues with GDI engines is their ability to maintain stable mixture stratification. Therefore, modern GDI engines are characterized by tumble-dominated flow fields. The presence of a significant tumble motion early during the compression stroke is more effective in enhancing the turbulence intensity at the time of ignition, which is essential for compensating for the slow flame speed of a stratified mixture. This is mainly due to the breaking of the tumble motion into small structures that have a size of the order of the turbulence length scale, which increases the rate of transformation of kinetic energy into turbulence [20].

As a common practice, steady flow rigs have traditionally been used to determine integral flow parameters such as tumble or swirl ratio, gulp factor, flow coefficient, discharge coefficient, etc. [21]. With the advent of more sophisticated mixture flow strategies in engines to reduce emissions, there is a need to obtain more detailed information on flow characteristics such as turbulence structure and turbulent kinetic energy, as these parameters have a significant effect on the mixing process. Also, there is a pressing need for this detailed information to validate the more sophisticated modelling techniques such as large eddy simulation (LES) [22]. Some studies have been done in optical engines to obtain detailed flow structures but they suffered from two main drawbacks: one is that they are dependent on the combustion chamber geometry, and therefore are not generic enough to allow an understanding of the fundamentals; the other, and more important, point is that they suffer from cycle to cycle variability. Thus, it is expected that the steady flow rig allows these studies independent of the interaction of the piston geometry and simplifies the problem by eliminating the dynamic effects of the running engine as a first step towards a deeper understanding of the flow characteristics.

Several measurement and visualization techniques have been used to study various aspects of the in-cylinder flow, mainly during the intake, compression, and combustion strokes of the four stroke GDI engines. In particular, the application of Particle Image Velocimetry (PIV) has seen an increase in application as it is the only method in non-intrusive fluid velocity metrology capable of providing a full field flow visualization and measurement of the characteristics of the unsteady complex in-cylinder flows [23]. B.M. Krishna investigated experimentally the in-cylinder tumble motion at different engine speeds utilizing Particle Image Velocimetry during the intake and compression strokes. The results illustrated that the tumble ratio was significantly changed with the crank angle, irrespective of the engine speed [24]. R.F. Huang [25] illustrated an experimental study to monitor the evolution and the destruction processes of the tumbling motion inside an internal combustion (IC) engine cylinder. The experiments were carried out during the intake and compression strokes using PIV. Furthermore, an inlet deflection-valve was used to control the deflection angle of the inlet flow. The results revealed that the strength of the tumble motion reached a maximum value between

120° and 180° crank angles, but decayed increasingly during the compression stroke. B.M. Krishna studied the in-cylinder flow pattern at different air flow rates under steady-state conditions and by maximum turbulent kinetic energy (TKE) and tumble ratio [26]. The results demonstrated that the tumble ratio increased with valve lift but was not much affected by the variation in air flow rates. It is generally acknowledged that proper enhancements of the mixture preparation process depend on a deep understanding of the in-cylinder flow characteristics obtained from PIV experiments. Recently, Proper Orthogonal Decomposition (POD) has been considered as a powerful, low-dimensional analysis technique for extracting information about the most dominant (coherent) and energetic structures of high-dimensional systems [27]. POD was firstly presented to the turbulence research by Lumley [28]. The source data for this technique can be either experimental PIV data, or numerical simulation data. Hanyang Zhuang implemented PIV experiments to measure the in-cylinder flow fields at different swirl ratios. Furthermore, a quadruple POD technique was applied to decompose the velocity fields into four parts: the dominant part, the coherent part, the turbulent part, and the noise part. The results revealed the strong relationship between the dominant structures and their kinetic energy and swirl ratios [29]. Tianyou Wang performed Large-eddy simulation (LES) to capture the instantaneous flow field of the in-cylinder flow of a GDI engine with the existence of a tumble flap in the intake port. POD decomposition was employed to gain a deep insight into the stochastic nature of the in-cylinder flow. The results showed that the strength of tumble motion increased and the cycle to cycle variation (CCV) decreased with the closed tumble flap compared to the open tumble flap. They concluded that the POD composition proved to be an efficient tool for an instantaneous velocity field decomposition [30]. Graham F. Pitcher carried out an important study to show the relation between the tumble generated on a steady-state flow rig and that generated in the cylinder of a motored engine using two different techniques, Laser Doppler Velocimetry (LDV) and PIV. The results demonstrated that there was reasonable agreement between the flow structures measured by LDV from the steady-state flow rig and the engine, and this was confirmed by a correlation coefficient. Moreover, the transient nature of the flow in the engine appeared to have little influence on the flow field [31].

The objective of the current paper is to characterize the in-cylinder air tumble motion under steady-state conditions. Full velocity vector maps were acquired in the vertical tumble plane (passing through the center of the cylinder), using PIV in a single optical cylinder, with four valves, a GDI head, and a flat piston at valve lifts of 1 mm, 5 mm, 9 mm, and 10 mm on a flow bench. The Proper Orthogonal Decomposition technique was implemented on the PIV data to extract the coherent structures impeded inside the in-cylinder flow. The combination of PIV-POD was expected to offer a better understanding of the air-fuel mixing.

## 2. Experimental Set Up

The experimental arrangement can be divided into two basic components: the steady-state flow bench and the PIV system.

### 2.1. Steady-State Flow Bench

Schematic diagram of the modified FEV (Forschungsgesellschaft für Energietechnik und Verbrennungsmotoren) steady-tumble rig used in the current study is shown in Figure 1. For steady-state measurements, air is inducted by a centrifugal compressor through the intake ports, cylindrical tube, and rotary piston gas meter. The two intake valves were manually adjusted using a micrometer and positioned at a constant valve-lift of 1 mm to 9 mm. The measurements were conducted at a constant pressure difference of 150 mmH<sub>2</sub>O across the intake valves. The pressure adjustment required for different valve lift settings was achieved by a stepper motor controlled by by-pass. The temperature and pressure of the intake air were measured by thermocouple and pressure transducer, respectively. The tumble level was gained by measuring the rotational speed of the paddle wheel anemometer. In the current study, a pent-roof, four valves GDI cylinder head was used, as shown

in Figure 2. A transparent cylinder liner was made of Plexiglas, having an internal bore diameter of 92.5 mm, stroke of 116 mm, and wall thickness of 3 mm. It was used to provide optical access through the full stroke length for PIV measurements. Two outlet ports with a recommended diameter of 35% of the bore diameter and a distance of 67 mm from the gas face were cut at both sides of the cylinder liner. A flat piston was placed at the bottom of the liner at the same distance of the engine stroke.

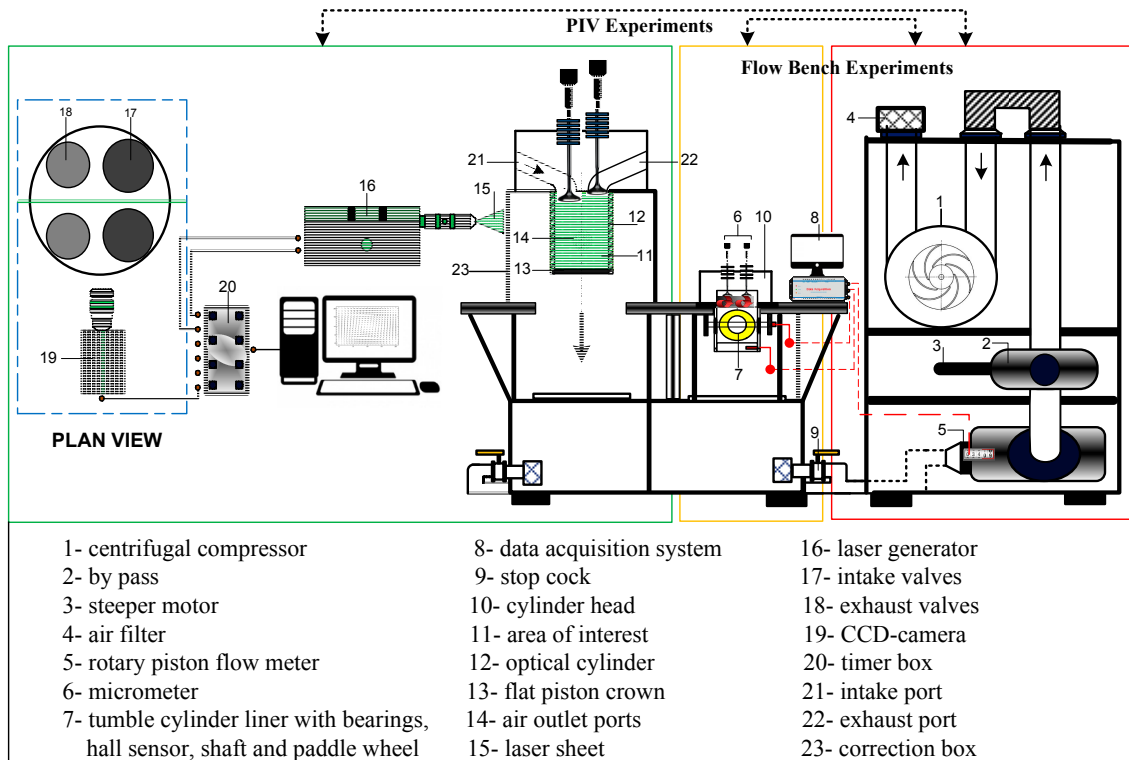


**Figure 1.** Schematic diagram for both flow bench and Particle Image Velocimetry (PIV) experiments.



**Figure 2.** Gasoline Direct Injection (GDI) cylinder head.

Parameters used in port performance analysis

- **Flow Coefficient**

The flow coefficient ( $C_f$ ) is the ratio between the experimentally obtained mass flow rate and the theoretical mass flow rate:

$$C_f = \frac{\dot{m}_{real}}{\dot{m}_{theor}} \quad (1)$$

The real mass flow rate was measured on the flow bench:

$$\dot{m}_{real} = Q \times \frac{P_1}{R \times T_1} \quad (2)$$

where:  $P_1$  is air pressure upstream of the valve,  $N/m^2$ ,  $T_1$  is air temperature upstream of the valve,  $K$ ,  $R$  is gas constant,  $J/Kg \cdot K$ , and  $Q$  is measured flow rate,  $m^3/s$ .

The theoretical mass flow rate ( $\dot{m}_{theor}$ ) for a defined cross sectional area ( $A_{Seat}$ ) was obtained as:

$$\dot{m}_{theor} = A_{Seat} \times \rho_s \times C_s \quad (3)$$

The flow velocity ( $C_s$ ) was calculated with the formula for isentropic flow:

$$C_s = \sqrt{\frac{2 \times k}{k-1} R \times T_1 \times \left[ 1 - \left( \frac{P_2}{P_1} \right)^{\frac{k-1}{k}} \right]} \quad (4)$$

where:  $P_2$  is air pressure downstream of the valve,  $N/m^2$ .

Likewise, the density under isentropic conditions was computed as:

$$\rho_s = \frac{P_1}{R \times T_1} \times \left( \frac{P_2}{P_1} \right)^{\frac{1}{k}} \quad (5)$$

#### • Coefficient of Discharge

The discharge coefficient ( $C_d$ ) is the ratio between the experimentally obtained mass flow rate and the theoretical mass flow rate:

$$C_d = \frac{\dot{m}_{real}}{\dot{m}_{theor}} \quad (6)$$

The theoretical mass flow rate ( $\dot{m}_{theor}$ ) for a defined orifice area between valve head and seat at different valve lifts ( $A_V$ ) was obtained as:

$$\dot{m}_{theor} = A_V \times \rho_s \times C_s \quad (7)$$

$$A_V = n \times \pi \times D_{seat}^2 \times \frac{L}{D} \times \cos \varnothing (1 + \frac{L}{D} \times \sin \varnothing \cdot \cos \varnothing) \quad (8)$$

where:  $L$  is valve lift,  $m$ ,  $n$  is the number of intake valves per cylinder,  $\varnothing$  is valve seat angle valve seat angle =  $45^\circ$ , and  $D_{seat}$  is the intake valve seat diameter,  $m$ .

#### • Non-Dimensional Rig Tumble

Non-dimensional rig-tumble is an indication to the tumble motion intensity and is indicated as a non-dimensional quantity  $C_T/C_A$ , where  $C_T$  is the circumferential velocity of the tumble motion, and  $C_A$  is the mean axial velocity in the cylinder.

The circumferential velocity of the tumble motion could be computed as follows:

$$C_T = 2 \times \pi \times N \times R_{MFL} \quad (9)$$

where:  $N$  is paddle wheel speed,  $R_{MFL}$  (mean paddle wheel radius) =  $0.36375 \times B$ , and  $B$  is the bore diameter,  $m$ .

The axial velocity of the air flow inside the cylinder could be calculated as follows:

$$C_T = \frac{\dot{m}_{real}}{\rho_{cyl} \times A_V} \quad (10)$$

$$\rho_{cyl} = \frac{P_2}{R \times T_2} \quad (11)$$

where:  $\rho_{cyl}$  is the air density inside the cylinder,  $kg/m^3$ .

## 2.2. PIV System

The experimental set-up of the PIV system consists of seeding particles, illumination source, imaging system, and PIV processor. The basic principle of PIV is to seed the flow with tracers and illuminate the area of interest with a thin sheet of laser light. The scattered light from the particles is recorded by means of a Charged Coupled Device (CCD) camera. If the time between the laser pulses is known, velocity magnitudes can be calculated from the distance travelled by each individual particle using cross correlation technique. The PIV analysis can be carried out in three different planes depending on the nature of the in-cylinder flow to be studied. The planes which are parallel to the cylinder axis and parallel to a line joining the inlet and exhaust valves are named tumble planes (Figure 3a). Planes perpendicular to the cylinder axis are called swirl planes and are viewed through the piston (Figure 3b). Finally, the planes parallel to the cylinder axis and perpendicular to the tumble planes are identified as cross-tumble planes (Figure 3c). In this study, 2D-PIV measurements were carried out at different valve lifts (1 mm, 5 mm, 9 mm, and 10 mm) in the mid-cylinder vertical tumble plane, i.e., plane of symmetry, as shown in Figure 4. The air flow was seeded at the intake port with Titanium Dioxide ( $\text{TiO}_2$ ) solid particles, which were generated by means of solid powder seeder. The light source used for this study was a doubled pulsed Nd: YAG laser (Dual Power 65-15) (Litron Lasers, Rugby, UK) with a wavelength of 532 nm, 15 Hz of maximum laser pulse frequency, and a capacity of 400 mJ/4 ns. The flow field of interest was illuminated twice with a time interval between pulses adjusted in the range of 125  $\mu\text{s}$ . Two hundred and eight pairs of images were acquired using a Flow Sense 2M Dantec Dynamics 8 bit digital output CCD camera with  $1600 \times 1200$  pixels running in double frame mode. The post processing of the acquired images was implemented using Dynamic studio V3.41 software (Dantec Dynamics, Skovlunde, Denmark). The evaluation was carried out using cross-correlation techniques with a  $64 \times 64$  pixels-sized interrogation area and 50% overlapping. After generating the raw velocity fields, a moving average validation and average filter techniques were applied to deal with the spurious (outliers) vectors. For PIV measurements, an acrylic correction box was designed to minimize the optical distortion caused by the curvature of the pipe, as shown in Figure 5.

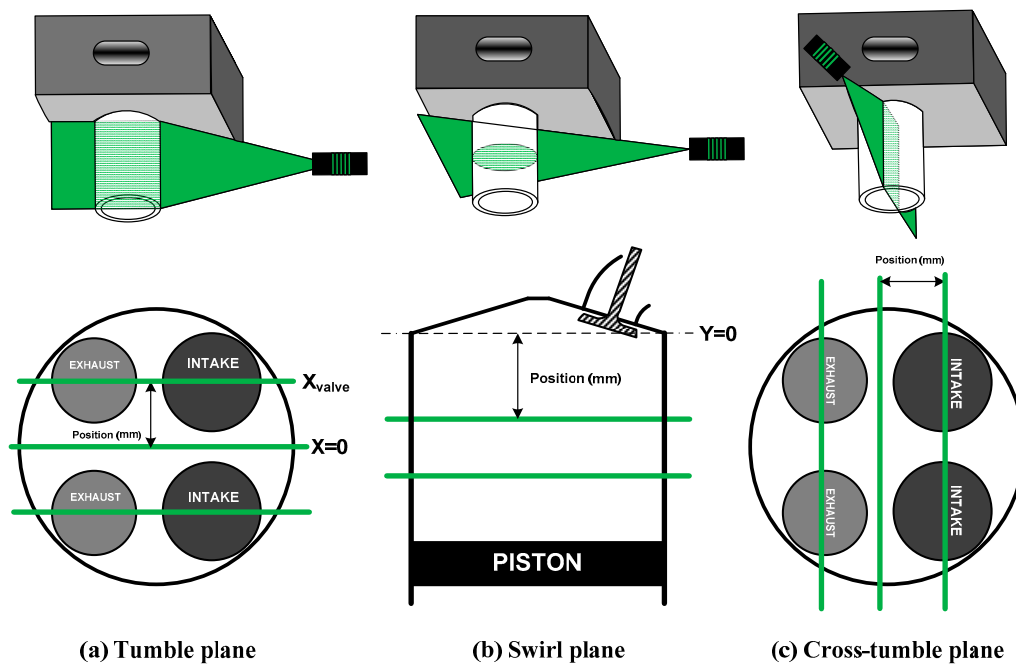


**Figure 3.** Particle Image Velocimetry (PIV) plane positions. (a) tumble planes; (b) swirl planes; (c) cross-tumble planes.

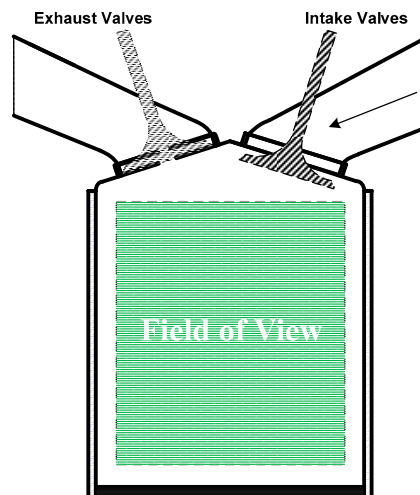


Figure 4. Schematic for the field of view.

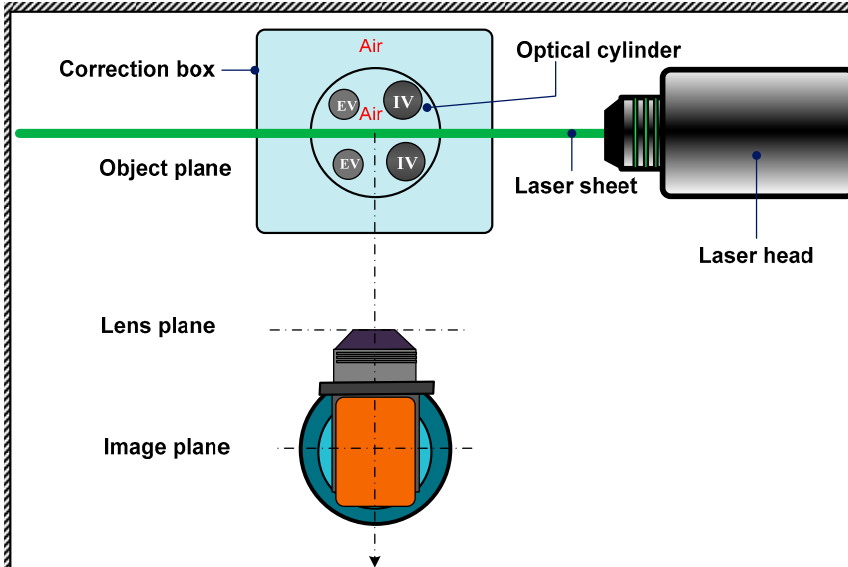


Figure 5. Top view of 2D-PIV camera configuration showing the correction box.

### 3. Proper Orthogonal Decomposition

The main idea behind POD is to decompose a set of velocity distributions (fluctuating velocity field)  $V^{(k)} = V^{(k)}(u, v)_{i,j}$  (called snapshots,  $k$  is the snapshot index and  $i, j$  are the index of grid points) into a linear combination of  $M$  spatial basis functions (space-dependent POD modes, denoted  $\phi_m^k$ ) and their corresponding time-dependent coefficients (denoted  $C_m^k$ ). The number of modes is equal to the number of snapshots, with the constraint that the POD modes are orthonormal to each other. The merit of this technique is that the most energetic coherent structures can be captured by using few POD modes.

$$V^{(k)} = \sum_{m=1}^M C_m^k * \phi_m^k \quad (12)$$

The mathematical procedures of the method of snapshot illustrated by Sirovich [32] are shown as follows:

- 1- The instantaneous velocity field ( $V$ ) must be decomposed firstly into two parts, the mean part ( $\bar{V}$ ) and the fluctuating part ( $V'$ ), as POD analysis is carried out only on the fluctuating part.

$$V = \bar{V} + V' \tag{13}$$

- 2- All fluctuating velocity components from the  $K$  snapshots are arranged in a matrix  $V$

$$V = \begin{bmatrix} u_{i=1,j=1}^{(1)} & u_{i=1,j=2}^{(1)} & \cdots & u_{i=1,j=J}^{(1)} \\ \vdots & \vdots & \vdots & \vdots \\ u_{i=I,j=1}^{(K)} & u_{i=I,j=2}^{(K)} & \cdots & u_{i=I,j=J}^{(K)} \\ v_{i=1,j=1}^{(1)} & v_{i=1,j=2}^{(1)} & \cdots & v_{i=1,j=J}^{(1)} \\ \vdots & \vdots & \vdots & \vdots \\ v_{i=I,j=1}^{(K)} & v_{i=I,j=2}^{(K)} & \cdots & v_{i=I,j=J}^{(K)} \end{bmatrix} \tag{14}$$

where  $K$  is the total number of snapshots and  $I*J$  are the number of total grid points in the velocity field.

- 3- Then, the spatial correlation matrix for velocity distributions is defined as

$$R = \frac{1}{K} (UU^T) \tag{15}$$

- 4- The corresponding eigenvalue problem is solved

$$R\phi_m = \lambda_m \phi_m \tag{16}$$

where  $\lambda_m$  and  $\phi_m$  are corresponding eigenvalues and vectors. Solutions are ordered according to the size of their eigenvalues, so that

$$\lambda_1 > \lambda_2 > \lambda_3 \dots \dots \dots \lambda_M = 0 \tag{17}$$

- 5- The POD modes ( $\phi_m^k$ ) are derived after normalization by projecting correlation matrix  $R$  onto the eigenvectors ( $\beta_m, m = 1, 2 \dots M$ ).
- 6- The corresponding coefficients ( $C_m^k$ ) of each mode are determined by projecting the original velocity fields onto the computed POD modes.
- 7- The kinetic energy captured by the  $m_{th}$  mode is calculated by

$$KE_m = \frac{1}{2} \sum_{k=1}^K (C_m^k)^2 \tag{18}$$

## 4. Results

### 4.1. Steady-State Flow Bench Results

Figure 6a shows the variation of the flow coefficient at different valve lifts. The flow coefficient increased with valve lift since the effective flow area through the valve increased. The figure also shows that the flow coefficient affected the engine breathing capacity significantly. In fact, the higher valve lift caused more air flow into the engine cylinder and thus higher engine breathing capacity, as shown in Figure 6b. The discharge coefficient, which is defined as the flow restriction made by valves and seat lips, depends entirely on the valve lift, as can be seen in Figure 6c. Since the inlet air jet was closed to the valve and its seat, the effect of viscous shear was prominent, especially at low valve lift. Accordingly, the discharge coefficient decreased due to the increase in the Reynolds number. The increase in Reynolds number could be attributed to the lower viscous effect of the jet at this condition. On the other hand, the flow broke away and made a free jet at high valve lifts.

This was mainly because of the fluid inertia that stopped the flow from rotating across the valve seat wall. Figure 6d shows the effect of the valve lift on the non-dimensional rig-tumble. Negative values, i.e., clockwise directions, were observed at lower valve lifts. These values could be explained by the abundant air that enters through the right side of the seat. Then, a symmetric flow distribution was observed at the valve seat area. This distribution occurred at roughly 5 mm without forming tumble motion. The distribution trend was observed again when the flow was shifted towards exhaust valves at high valve lifts. The deflection of the flat piston crown intensifies the distribution even more. A strong tumbling motion formed by the jet flow was noticed inside the cylinder. This motion was of positive values, that is, counterclockwise direction.

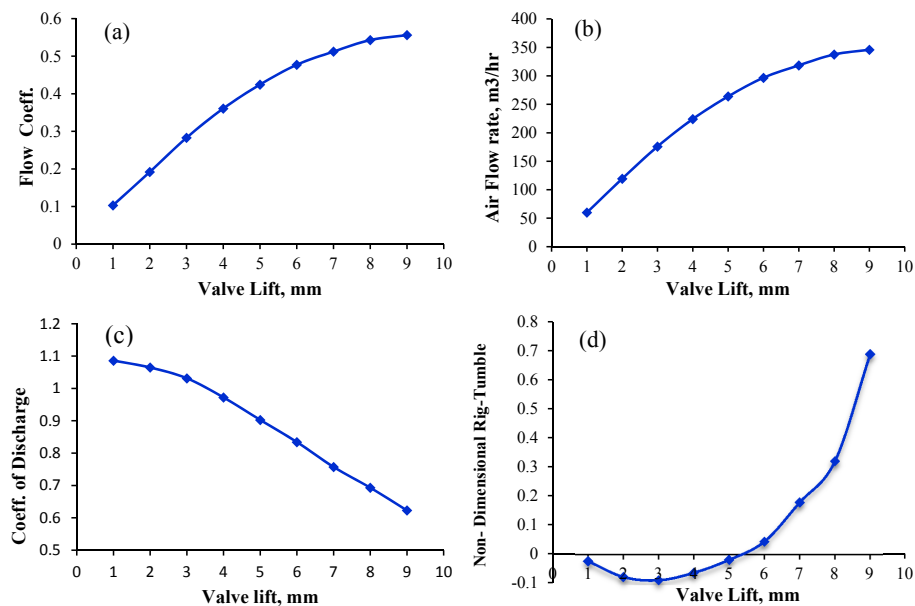


**Figure 6.** Integral flow parameters variation versus valve lift. (a) flow coefficient; (b) air flow rate; (c) discharge coefficient; (d) non-dimensional rig-tumble.

#### 4.2. PIV Measurements in the Tumble Plane

The in-cylinder flow fields at the mid cylinder plane, for different valve lifts, are shown in Figure 7. The velocity fields are represented by the vectors (arrows), whose lengths are proportional to the ensemble average velocity, and directions are specified by the orientation of the arrows. Actually, high tumble motion is usually achieved by using straight ports oriented in such a way that most of the annular jet exiting the inlet valves is directed towards the exhaust side. It can be noticed from Figure 7 that at lower valve lifts more air entered into the cylinder from the right side of the intake valve, forming a jet almost parallel to the cylinder wall. Subsequently, the area under the intake valves was the area where the maximum velocities were concentrated. In a similar way, a small amount of air entered into the cylinder from the left side towards the exhaust valves and was deflected by the cylinder wall towards the right bottom side of the cylinder, forming another jet. The right-side jet domination might explain the rotation of the paddle wheel during steady-state experiments in a clockwise direction, with negative lower tumble ratios until 5 mm valve lift. At 5 mm valve lift, it can be seen that the two jets are identical due to symmetric flow coming from both sides of the intake valves. Moreover, there was a symmetrical velocity distribution in the middle of the cylinder that might explain the rotation stoppage of paddle wheel at this valve lift. By increasing the valve lift more, it can be noticed that the maximum velocity concentration transferred to the left side (exhaust side) due to more air entering from the left side. The interaction of this dominant jet with the flat piston formed a counterclockwise vortex with a center near to the lower bottom right side. By increasing the valve lift more, the vortex became clearer and its center shifted towards the center of the cylinder.

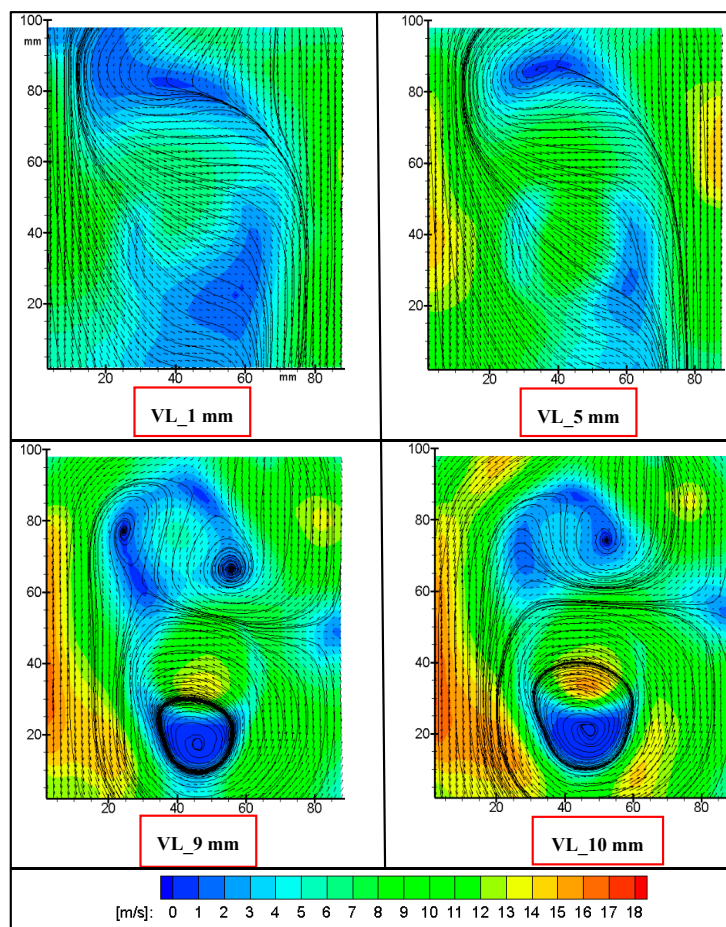


Figure 7. Ensemble-averaged velocity vectors at different valve lifts.

Figure 8 illustrates the vorticity magnitudes at different valve lifts. Vorticity is the rotational rate of the fluid. For a three dimensional vector field the vorticity is defined by:

$$\text{curl } V = \nabla \times V = \left( \frac{\partial v_z}{\partial y} - \frac{\partial v_y}{\partial z} \right) \vec{i} + \left( \frac{\partial v_x}{\partial z} - \frac{\partial v_z}{\partial x} \right) \vec{j} + \left( \frac{\partial v_y}{\partial z} - \frac{\partial v_{zx}}{\partial y} \right) \vec{k}$$

where  $V$  is the velocity vector and  $\vec{i}$ ,  $\vec{j}$ , and  $\vec{k}$  are the unit vectors in  $x$ ,  $y$ , and  $z$  axis.

Blue area represents the clockwise rotation (negative values), while green area represents the counterclockwise rotation (positive values). Significant differences can be found between lower and higher valve lifts. At 2 mm valve lift, the strength of vortices was higher in clockwise direction behind the intake valves (negative tumble motion). At 5 mm valve lift, there was balance in vorticity magnitude between negative and positive values because of the symmetrical velocity distribution between both jets coming from both sides of the intake valves. At high valve lifts, significant amount of the incoming flow was directed towards the exhaust side, which made the air jet coming from the left side of the intake valve-dominant. This led to the formation of strong tumble vortices in counterclockwise direction, which dominated the in-cylinder flow.

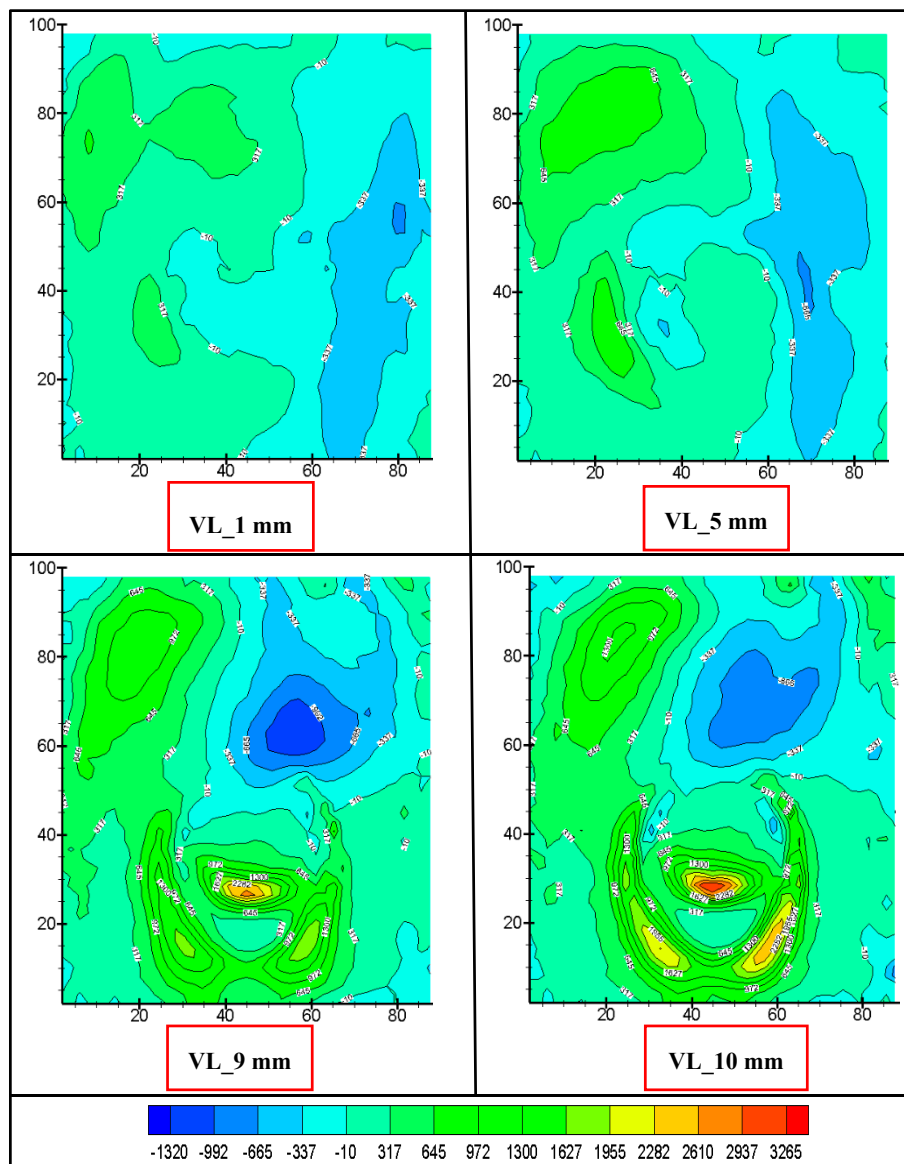
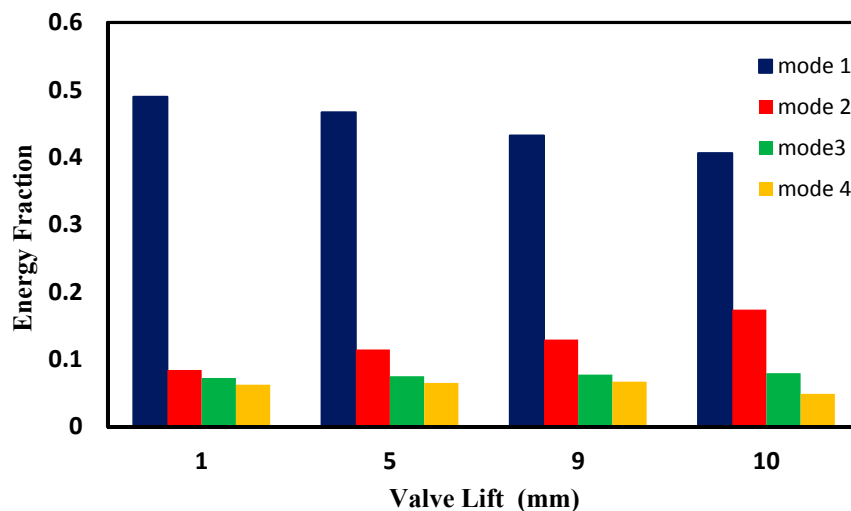


Figure 8. Vorticity magnitudes at different valve lifts.

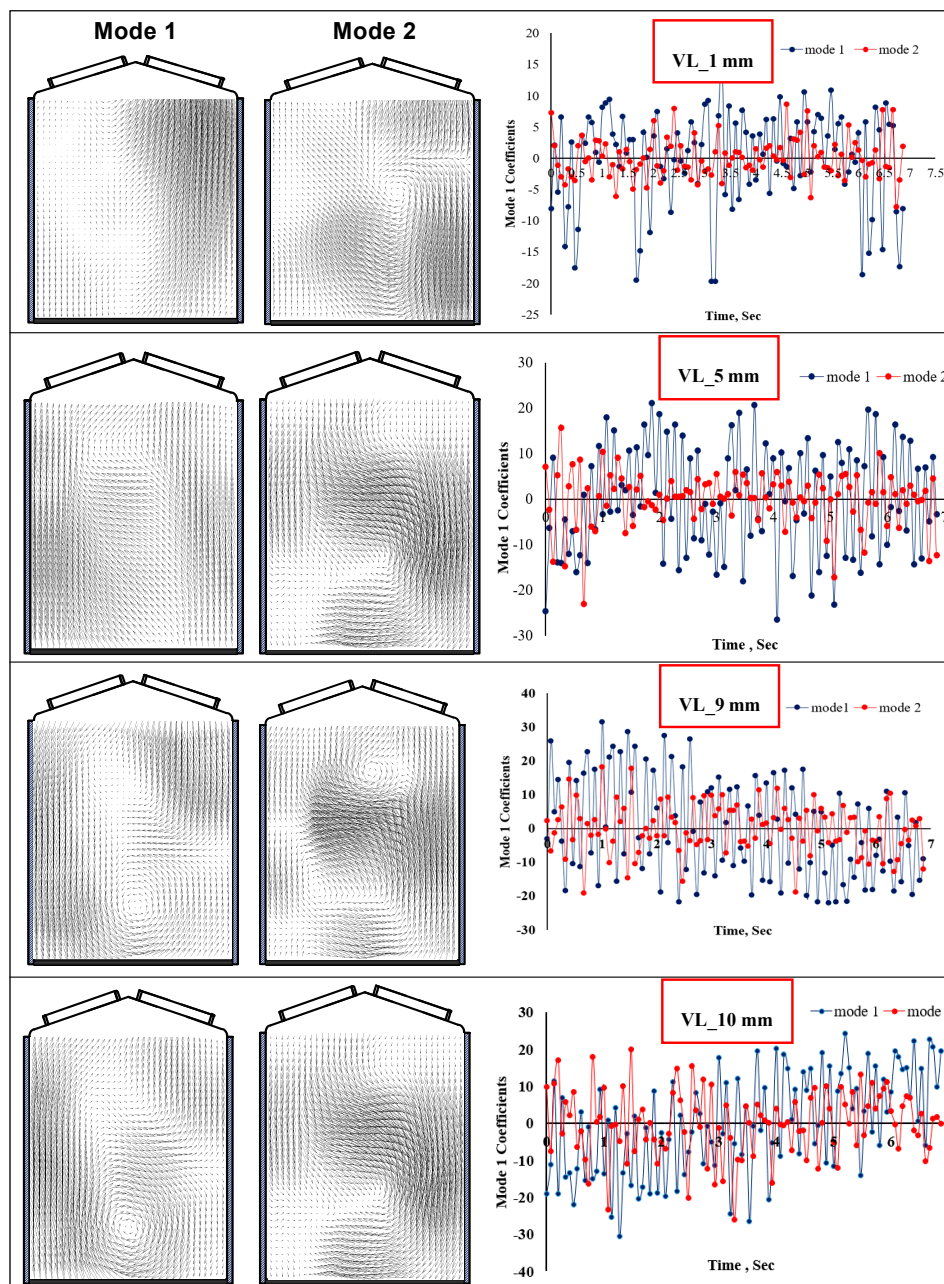
#### 4.3. POD Results

Figure 9 presents the energy fraction captured by the first five POD modes at different valve lifts in order to determine the contribution of each mode to the original flow field. Only five modes were calculated, as they mainly contain the dominant flow field structures. As can be seen from the figure that mode 1 contained about 48.9%, 46.6%, 43.2%, and 40.6% of the turbulent kinetic energy for 1 mm, 5 mm, 9 mm, and 10 mm valve lifts, respectively. This significantly demonstrated that mode 1 was capable of capturing the most coherent structures. It can also be seen that the contribution of first mode for valve lift 1 was more than for valve lift 10, indicating that some of the flow energy cascaded towards higher order modes, which represent small-scale structures.



**Figure 9.** Energy fraction captured by first five Proper Orthogonal Decomposition (POD) modes at different valve lifts.

The first two POD modes and their corresponding time-dependent coefficients for different valve lifts are shown in Figure 10. As can be seen from the figure, each POD mode contained a particular physical flow structure, while the magnitude of the time-dependent coefficients for a specific POD mode illustrated to what extent this mode was dominant for every snapshot. As expected from the steady-state experiments, the first mode for valve lift 1 mm showed the domination of a right-jet-like structure behind the intake valves. A flow structure can also be located at the exhaust valve, while the flow pattern in the second mode identified a large-scale coherent structure. Therefore, the combination of the two mode structure might explain the rotation of the paddle wheel in the clockwise direction with a negative, non-dimensional tumble-rig at lower valve lifts. Coefficients for POD modes 1 and 2 oscillated between positive and negative values and, as expected, the amplitude for coefficient mode 1 was greater than mode 2. Spatial modes combined with coefficients highlight the contribution of the particular mode to the actual flow field. From Figure 8, it was concluded that POD spatial mode 1 and its coefficient correlate directly to the negative tumble motion. For 5 mm valve lift, the first mode identified the flow pattern in which the velocity vectors were moving from bottom to top of the cylinder. A large-scale coherent structure was absent in this mode, indicating the absence of tumble motion. The higher coefficient values of mode 1 indicated a strong contribution from this spatial mode in the corresponding snapshot. Zero coefficient value in a particular snapshot represented no contribution. For 9 mm valve lift, the first mode identified a clockwise, rotating, large-scale, coherent structure near the lower half of the cylinder. This mode 1 flow pattern appeared due to the formation of a strong positive-tumble motion. The second POD mode also captured a clockwise rotating coherent structure, but in the upper half of the cylinder. The amplitude of the coefficient of mode 1 was very high, indicating the positive-tumble motion. It was also noticed that after half the number of snapshots, the coefficient values for mode 1 started to become negative, whereas the coefficient of the second mode had a lower amplitude than the first mode, indicating a smaller contribution of spatial mode 2 to the original flow field. Finally, for 10 mm valve lift, the first POD mode captured a strong, clockwise, rotating coherent structure in the lower half of the cylinder, indicating the strong positive-tumble motion. Interestingly, the coefficient values for mode 1 started to increase from negative to positive after half the number of snapshots. The important flow field feature identified in mode 2 was a region of low (or zero) velocity vectors extending from the bottom left side to the middle of the cylinder. It created a point of stagnation where velocity vectors coming from the left side interacted with a streak coming from the right.



**Figure 10.** Mode 1 and mode 2 structures and their corresponding coefficients at different valve lifts.

The reconstruction of the original velocity fields was performed for valve lifts 9 mm and 10 mm using the first five dominant modes, as shown in Figure 11. The reason for selecting only the first five modes was the fact that they contained 76.5% and 74.4% of the total energy for valve lift 9 mm and 10 mm, respectively. The reconstructed flow field for valve lift 9 mm successfully identified a dominant coherent structure at the bottom of the cylinder and a pair of clockwise and counterclockwise rotating coherent structures in the upper half of the cylinder. All these flow patterns were in full agreement with the ensemble average field. The reconstruction of the velocity field for valve lift 10 mm also identified the same flow features, as witnessed in the ensemble average velocity field. It was concluded that the first five modes were sufficient for the reconstruction of the flow field, which also provided validation for the POD results.

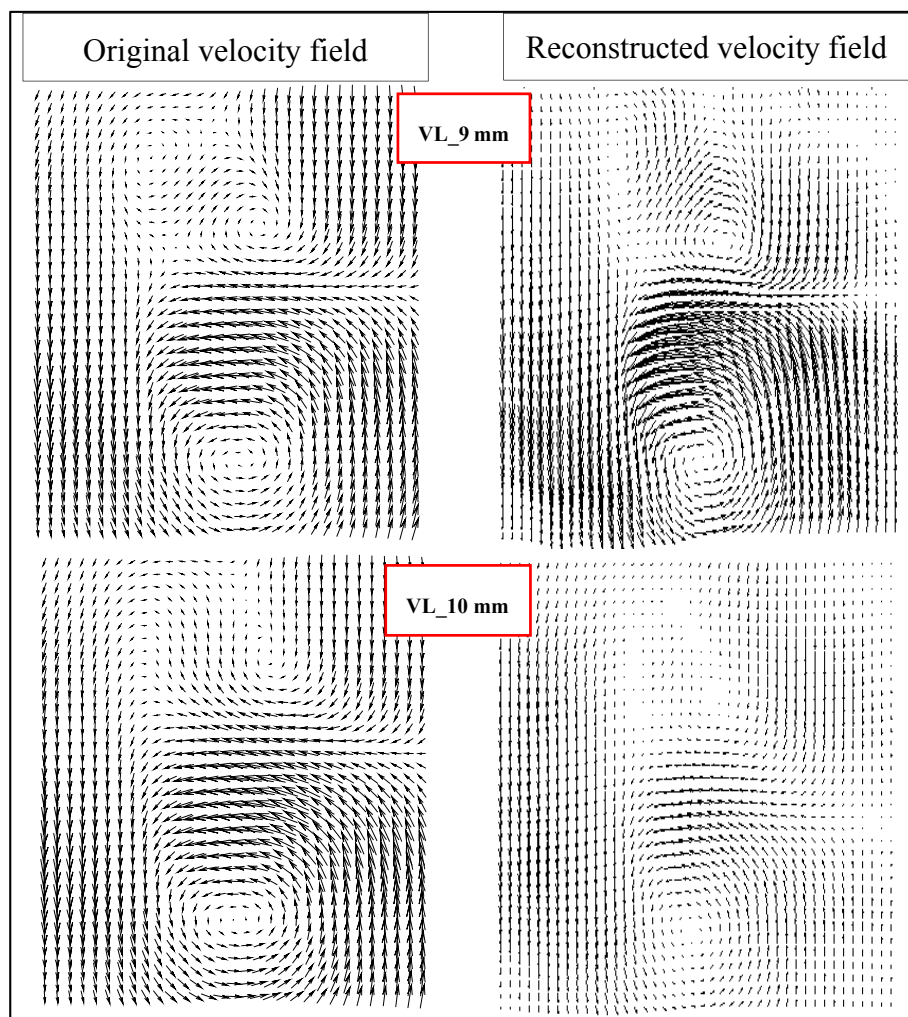


Figure 11. Reconstructed velocity field versus original velocity field for 9 mm and 10 mm valve lifts

## 5. Conclusions

An experimental study was carried out to characterize the in-cylinder flow of the Gasoline Direct Injection (GDI) engine under steady-state conditions using Particle Image Velocimetry (PIV). The experiments were carried out on a four-valve, pent-roof GDI engine head at different valve lifts and a pressure difference of 150 mmH<sub>2</sub>O across the intake valves. Proper Orthogonal Decomposition (POD) was applied on the PIV data in order to extract the coherent structures impeded inside the in-cylinder flow and hence gain an understanding of the air-fuel mixing. The following conclusions were drawn from the current study:

- The steady-state experiments illustrated that at low valve lifts, the high velocity vectors were concentrated behind the intake valves. At about 5 mm, the valve lift of the velocity distribution was symmetrical, resulting in no tumble motion. At high valve lifts, a significant amount of the incoming air to the cylinder was directed towards the exhaust side, forming a strong jet from the left side of the valve seat. The interaction of this air jet with the left cylinder wall and then with the flat piston led, finally, to a strong tumbling motion within the cylinder, with positive values of the non-dimensional tumble-rig.
- The PIV ensemble-average velocity distribution showed a good qualitative agreement with the measured, steady-state-flow integral parameters.

- POD results showed that mode 1 contained about 48.9%, 46.6%, 43.2%, and 40.6% of the turbulent kinetic energy for the 1 mm, 5 mm, 9 mm, and 10 mm valve lifts, respectively. It was observed that, at high valve lifts, some of the energy in the large eddies of mode 1 was transferred to the smaller flow structures of modes 2 and 3.
- The reconstructed flow field using the first five dominant modes for both valve lifts (9 mm and 10 mm) were in agreement with the ensemble average field.
- The combination between 2-D PIV and POD provided good information about the flow structure and the relative energy content in the various modes.

**Acknowledgments:** Financial support by the Universiti Teknologi PETRONAS through the Centre for Automotive Research and Energy Management (CAREM) is highly appreciated. We need also to acknowledge the contribution of Ricardo UK for providing the cylinder head and its characteristics.

**Author Contributions:** The investigation was supervised by Morgan Heikal and A. Rashid. The experimental work and analysis and most illustrations were conducted by Mohammed El Adawy. M. I. Siddiqui and S. Munir contributed in data analysis and the preparation of the experimental set up.

**Conflicts of Interest:** The authors declare no conflict of interest.

## References

1. Zhao, F.; Lai, M.-C.; Harrington, D.L. Automotive spark-ignited direct-injection gasoline engines. *Prog. Energy Combust. Sci.* **1999**, *25*, 437–562. [[CrossRef](#)]
2. Smith, J.D.; Sick, V. *A Multi-Variable High-Speed Imaging Study of Ignition Instabilities in a Spray-Guided Direct-Injected Spark-Ignition Engine*; SAE Technical Paper 0148-7191; SAE International: Troy, MI, USA, 2006.
3. Kume, T.; Tanada, H.; Iida, K.; Murakami, N.; Ando, H. Combustion control technologies for direct injection SI engines. *JSAE Rev.* **1996**, *4*, 435.
4. Spiegel, L.; Spicher, U. *Mixture Formation and Combustion in a Spark Ignition Engine with Direct Fuel Injection*; SAE Technical Paper 0148-7191; SAE International: Troy, MI, USA, 1992.
5. Preussner, C.; Döring, C.; Fehler, S.; Kampmann, S. *GDI: Interaction between Mixture Preparation, Combustion System and Injector Performance*; SAE Technical Paper 0148-7191; SAE International: Troy, MI, USA, 1998.
6. Fraidl, G.; Piock, W.; Wirth, M. *Gasoline Direct Injection: Actual Trends and Future Strategies for Injection and Combustion Systems*; SAE Technical Paper 0148-7191; SAE International: Troy, MI, USA, 1996.
7. Yamakawa, M.; Isshiki, S.; Lee, J.; Nishida, K. *3-D PIV Analysis of Structural Behavior of DI Gasoline Spray*; SAE Technical Paper 0148-7191; SAE International: Troy, MI, USA, 2001.
8. Lee, J.; Yamakawa, M.; Isshiki, S.; Nishida, K. *An Analysis of Droplets and Ambient Air Interaction in a DI Gasoline Spray Using LIF-PIV Technique*; SAE Technical Paper 0148-7191; SAE International: Troy, MI, USA, 2002.
9. Ishida, R.; Nakayama, T.; Kaneko, M.; Morikawa, K. *Analysis of In-Cylinder Flow and Fuel Vapor Concentration Distribution in Gasoline Direct Injection Engine*; SAE Technical Paper 0148-7191; SAE International: Troy, MI, USA, 2011.
10. Hung, D.L.; Zhu, G.G.; Winkelmann, J.R.; Stuecken, T.; Schock, H.; Fedewa, A. *A High Speed Flow Visualization Study of Fuel Spray Pattern Effect on Mixture Formation in a Low Pressure Direct Injection Gasoline Engine*; SAE Technical Paper 0148-7191; SAE International: Troy, MI, USA, 2007.
11. Serras-Pereira, J.; Aleiferis, P.; Richardson, D.; Wallace, S. *Mixture Preparation and Combustion Variability in a Spray-Guided DISI Engine*; SAE Technical Paper 0148-7191; SAE International: Troy, MI, USA, 2007.
12. Banerjee, R.; Kumar, S. Numerical investigation of stratified air/fuel preparation in a GDI engine. *Appl. Therm. Eng.* **2016**, *104*, 414–428. [[CrossRef](#)]
13. Georjon, T.; Bourguignon, E.; Duverger, T.; Delhay, B.; Voisard, P. *Characteristics of Mixture Formation and Combustion in a Spray-Guided Concept Gasoline Direct Injection Engine: An Experimental and Numerical Approach*; SAE Technical Paper 0148-7191; SAE International: Troy, MI, USA, 2000.
14. Gold, M.; Li, G.; Sapsford, S.; Stokes, J. *Application of Optical Techniques to the Study of Mixture Preparation in Direct Injection Gasoline Engines and Validation of a CFD Model*; SAE Technical Paper 0148-7191; SAE International: Troy, MI, USA, 2000.

15. Lucchini, T.; D'Errico, G.; Onorati, A.; Bonandrini, G.; Venturoli, L.; di Gioia, R. *Development of a CFD Approach to Model Fuel-Air Mixing in Gasoline Direct-Injection Engines*; SAE Technical Paper 0148-7191; SAE International: Troy, MI, USA, 2012.
16. Heywood, J. *Internal Combustion Engine Fundamentals*; McGraw-Hill Education: New York, NY, USA, 1988.
17. Ricardo, J. *Steady State Flow Bench Port Performance Measurement and Analysis Techniques*; Report DP93/0704; Ricardo: Shoreham-by-Sea, UK, 1993.
18. Hill, P.; Zhang, D. The effects of swirl and tumble on combustion in spark-ignition engines. *Prog. Energy Combust. Sci.* **1994**, *20*, 373–429. [[CrossRef](#)]
19. El-Adawy, M.; Heikal, M.; Aziz, A.R.A.; Siddiqui, M.; Wahhab, H.A.A. Experimental study on an IC engine in-cylinder flow using different steady-state flow benches. *Alex. Eng. J.* **2017**. [[CrossRef](#)]
20. Khalighi, B. Study of the intake tumble motion by flow visualization and particle tracking velocimetry. *Exp. Fluids* **1991**, *10*, 230–236. [[CrossRef](#)]
21. Yang, X.; Kuo, T.-W.; Guralp, O.; Grover, J.R.O.; Najt, P. In-Cylinder Flow Correlations between Steady Flow Bench and Motored Engine Using Computational Fluid Dynamics. *J. Eng. Gas Turbines Power* **2017**, *139*, 072802. [[CrossRef](#)]
22. Baratta, M.; Misul, D.; Spessa, E.; Viglione, L.; Carpegna, G.; Perna, F. Experimental and numerical approaches for the quantification of tumble intensity in high-performance SI engines. *Energy Convers. Manag.* **2017**, *138*, 435–451. [[CrossRef](#)]
23. Reuss, D.L.; Adrian, R.J.; Landreth, C.C.; French, D.T.; Fansler, T.D. *Instantaneous Planar Measurements of Velocity and Large-Scale Vorticity and Strain Rate in an Engine Using Particle-Image Velocimetry*; SAE Technical Paper 0148-7191; SAE International: Troy, MI, USA, 1989.
24. Krishna, B.M.; Mallikarjuna, J. Effect of engine speed on in-cylinder tumble flows in a motored internal combustion engine—An experimental investigation using particle image velocimetry. *J. Appl. Fluid Mech.* **2011**, *4*, 1–14.
25. Huang, R.; Huang, C.; Chang, S.; Yang, H.; Lin, T.; Hsu, W. Topological flow evolutions in cylinder of a motored engine during intake and compression strokes. *J. Fluids Struct.* **2005**, *20*, 105–127. [[CrossRef](#)]
26. Krishna, B.M.; Mallikarjuna, J. Characterization of flow through the intake valve of a single cylinder engine using particle image velocimetry. *J. Appl. Fluid Mech.* **2010**, *3*, 23–32.
27. Munir, S.; Siddiqui, M.I.; Heikal, M.; Aziz, A.R.A.; de Sercey, G. Identification of dominant structures and their flow dynamics in the turbulent two-phase flow using POD technique. *J. Mech. Sci. Technol.* **2015**, *29*, 4701–4710. [[CrossRef](#)]
28. Lumley, J.L. The structure of inhomogeneous turbulent flows. *Atmos. Turbul. Radio Wave Propag.* **1967**, *790*, 166–178.
29. Zhuang, H.; Hung, D.L. Characterization of the effect of intake air swirl motion on time-resolved in-cylinder flow field using quadruple proper orthogonal decomposition. *Energy Convers. Manag.* **2016**, *108*, 366–376. [[CrossRef](#)]
30. Wang, T.; Li, W.; Jia, M.; Liu, D.; Qin, W.; Zhang, X. Large-eddy simulation of in-cylinder flow in a DISI engine with charge motion control valve: Proper orthogonal decomposition analysis and cyclic variation. *Appl. Therm. Eng.* **2015**, *75*, 561–574. [[CrossRef](#)]
31. Pitcher, G. An Investigation and Comparison between Standard Steady Flow Measurements and Those in a Motored Engine. Ph.D. Thesis, Loughborough University, Loughborough, UK, 2013.
32. Sirovich, L. Chaotic dynamics of coherent structures. *Phys. D Nonlinear Phenom.* **1989**, *37*, 126–145. [[CrossRef](#)]

